Article

Sol–Gel-Processed Y2O3 Multi-level Resistive Memory Cells for Neural Networks

Taehun Lee , Hae-In Kim , Yoonjin Cho , Sangwoo Lee , Won-Yong Lee , Jin-Hyuk Bae [*] , In Man Kang , Kwangeun Kim , Sin-Hyung Lee [*] , Jaewon Jang [*]

Article

Sol–Gel-Processed Y2O3 Multi-level Resistive Memory Cells for Neural Networks

Taehun Lee [1], Hae-In Kim [1], Yoonjin Cho [1], Sangwoo Lee [1], Won-Yong Lee [1,2], Jin-Hyuk Bae [1], In-Man Kang [1], Kwangeun Kim [3], Sin-Hyung Lee [1,*] and Jaewon Jang [1,*]

[1]   School of Electronic and Electrical Engineering, Kyungpook National University, Daegu 41566, Korea; lth0313@knu.ac.kr (T.L.); khi5735@knu.ac.kr (H.I.K.); sangw98@knu.ac.kr (S.L); yongsz@knu.ac.kr (W.Y.L.)

[2]   The Institute of Electronic Technology, Kyungpook National University, Daegu 41566, Korea; kke@kau.ac.kr (K.K.)

[3]   School of Electronics and Information Engineering, Korea Aerospace University, Goyang10540, Korea

*   Correspondence: sinhlee@knu.ac.kr (S.H.L); j1jang@knu.ac.kr (J.J.)

Abstract: Yttrium oxide (Y_2O_3) resistive random-access memory (RRAM) devices were fabricated using the sol–gel process on indium tin oxide/glass substrates. These devices exhibited conventional bipolar RRAM characteristics, without requiring a high voltage forming process. The effect of current compliance on the Y_2O_3 RRAM devices was investigated and revealed that as the set current compliance values increased, the resistance values gradually decreased. Consequently, intermediate resistance values were obtained, which are suitable for multi-level cell (MLC) switching. The fabricated Y_2O_3 RRAM devices were capable of functioning as an MLC with a capacity of 2 bits in one cell, utilizing three low resistance states and one common high resistance state. The potential of the Y_2O_3 RRAM for neural networks was further explored through numerical simulations. Hardware neural networks based on the Y_2O_3 RRAM demonstrated effective digit image classification with a high accuracy rate of approximately 88%, comparable to the ideal software-based classification (~92%). This suggests that the proposed RRAM has the potential to be utilized as a memory component in practical neuromorphic systems.

Keywords: sol-gel; Y_2O_3; RRAM; multi level cell

1. Introduction

Non-volatile resistive random-access memory (RRAM) is considered a crucial element for the next generation of memory technologies. RRAM, with its simple sandwich structure, offers high-speed performance, low power consumption, and exceptional scalability. These advantages help overcome the von Neumann bottleneck and pave the way for neuromorphic computing systems, which aim to mimic the data processing capabilities of the human brain [1–3]. To accommodate large amounts of data within a limited substrate area, the density of memory devices must be significantly increased. Various approaches, such as complex 3D structures such as vertical RRAM or crossbar configurations, have been proposed to achieve higher storage density [4]. However, these methods often entail complex and costly fabrication processes. Alternatively, a simpler approach is to enable multi-level cell operation with a single memory device. Furthermore, in the context of neuromorphic systems that rely on parallel computation, it is essential to emulate biological synapses, which possess analog weight values. In terms of integration density, a non-volatile memory component with multi-level memory capabilities is better suited to simulate synapses in neuromorphic systems compared with typical digital memory devices.

Numerous metal oxide materials, including ZrO_2, HfO_2, TiO_2, and Y_2O_3, have been utilized as active channel layers in RRAM devices [5–15]. Among them, Y_2O_3 stands out due to its high dielectric constant and large optical band gap, making it a promising high-k candidate for replacing SiO_2 in complementary metal–oxide-semiconductor processes in the industry. The fast ion movement within Y_2O_3 enables rapid RRAM operation. For integrated RRAM arrays, the "sneak path" issue must be addressed. One solution is to combine Y_2O_3 with a transistor, acting as a selector. Y_2O_3 layers can also

serve as a passivation layer for transistors, ensuring stable operation, while simultaneously functioning as an active channel layer for RRAM devices. This approach reduces the number of fabrication steps and enhances cost efficiency [16,17]. Various conventional vacuum-based deposition methods have been used to deposit metal oxide active channel layers. However, these methods are time-consuming and not cost-efficient. In contrast, the sol–gel process is a well-known technique for depositing metal oxide layers using solution-phase precursor solutions. These precursor solutions can be used as ink for printing or spin-coating, allowing for large area application at a lower cost [18,19].

In this study, sol–gel-processed Y_2O_3 films were employed as active channel layers for RRAM devices. The fabricated Y_2O_3 RRAM devices exhibited conventional bipolar memory operation without requiring a forming process, thanks to the presence of oxygen vacancies with top Ag electrodes. These devices showed a sharp transition from a high resistance state (HRS) to a low resistance state (LRS) or vice versa. To enable multi-cell operation, the set current compliance was varied. As the current compliance values increased, the resistance values obtained gradually decreased, resulting in intermediate values within the LRS and HRS, suitable for multi-level cell (MLC) switching. In numerical simulations, the Y_2O_3 RRAM device with multi-level memory states effectively functioned as an artificial synaptic cell for hardware neural networks. The constructed neuromorphic system achieved successful recognition of complex hand written digit images with an accuracy of approximately 88%. This level of accuracy is comparable to that of an ideal software system.

2. Materials and Methods

Y_2O_3 RRAM devices were fabricated using a vertically stacked structure, comprising glass, indium tin oxide (ITO) bottom electrodes, Y_2O_3, and Ag top electrodes (TEs). The fabrication process involved several steps:

Cleaning the ITO-coated glass substrate: The substrate was immersed in acetone and sonicated for 10 min, followed by additional cleaning with deionized water. UV/O_3 treatment was then performed for 1 h to remove any remaining organic impurities.

Y_2O_3 precursor solution preparation: A Y_2O_3 precursor solution (0.3 M) was created by dissolving yttrium (III) nitrate tetrahydrate $(Y(NO_3)_34H_2O)$ in 2-methoxymethanol. The solution was sonicated for an additional 10 min to achieve a clear solution.

Coating Y_2O_3 on the ITO/glass substrate: A tiny Kapton tape was used to define the contact window for the ITO bottom electrodes. The Y_2O_3 precursor solution was then spin-coated onto the cleaned ITO/glass substrate at 3000 rpm for 50 s. The Kapton tape was removed before the heating process.

Thermal annealing: To evaporate the solvent, the coated substrate was annealed on a hot plate at 100°C for 10 minutes. The coated substrate was thermally annealed in a furnace at 500°C for 3 h in the presence of air to convert the Y_2O_3 precursor into Y_2O_3.

Deposition of Ag TE: A shadow metal mask was placed in contact with the Y_2O_3 film to define the size of the electrode (30 μm × 30 μm). A 100 nm thick layer of Ag was deposited onto the Y_2O_3 films using thermal evaporation at a rate of 1.8 Å/s under 5×10^{-6} torr.

After fabrication, the crystal structure properties of the Y_2O_3 film were investigated using grazing incidence X-ray diffraction (GIXRD) with $CuK\alpha$ radiation. Japan). The optical characteristics of the sol-gel processed films were estimated by UV–visible technique (UV–vis; LAMBDA 265, MA, USA) A field-emission scanning electron microscope (SEM, S-4800, Hitachi, Cold type) was used to estimate the thickness and surface roughness of the film. The chemical composition analysis was conducted using X-ray photoelectron spectroscopy (XPS). The electrical characteristics, including I–V curve, retention, and endurance, were measured at room temperature using a probe station (MST T-4000A) and parameter analyzer (Keithley 2636B).

3. Results and Discussion

Figure 1a displays the GIXRD spectra of the Y_2O_3 film fabricated through the sol–gel method. The diffraction peaks at 2θ angles of 29.30°, 33.96°, 48.79°, and 57.93° correspond to the (222), (400), (440), and (622) crystallographic planes of Y_2O_3, respectively. Based on the GIXRD results, it is evident that the fabricated Y_2O_3 film consists entirely of a cubic crystal structure in the polycrystalline phase, specifically conforming to the cubic Y_2O_3 phase (JCPDS 74-1828). Notably, while a metastable monoclinic Y_2O_3 phase can form at low temperatures, the dominant phase observed here is the stable cubic Y_2O_3 phase [20]. The presence of the prominent peak at 29.30° indicates that the grains in the film primarily grow in the (222) plane. The crystallite size of the grains can be determined using the Scherrer equation.

$$D = (0.9\,\lambda) / (\beta \cos \theta), \tag{1}$$

where D, λ, β, and θ represent the crystalline size, CuKα wavelength, full width at half maximum (FWHM) of the diffraction peak, and Bragg angle, respectively. The grain size of the (222) plane is the largest among the crystallographic planes, which is evident from the narrowest FWHM of the diffraction peak at 29.30°. The calculated crystalline size from the (222) plane is determined to be 12.23 nm.
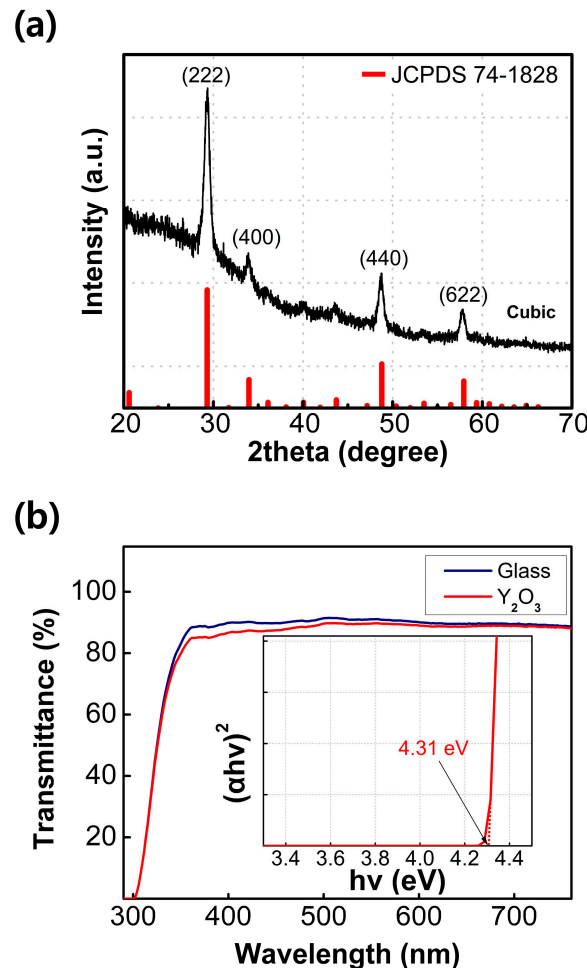
(a)

(b)

Figure 1. (**a**) GIXRD spectra of sol–gel-processed Y_2O_3 films and (**b**) transmittance spectra of sol–gel-processed Y_2O_3 films; the inset shows (ahv)^2 vs. photon energy.

The optical characteristics of the Y_2O_3 film were investigated via ultraviolet–visible spectroscopy (UV–Vis). As shown in Figure 1b, the fabricated film shows similar transmittance spectrum to that of the cleaned glass sample in the visible range, implying sufficient transparency of the fabricated film.

The bandgap of the Y_2O_3 film can be obtained by extrapolating the linear part of the $(ahv)^2$ versus hv graph. The inset of Figure 1b shows the $(ahv)^2$ versus hv derived from the Tauc equation.

$$(ahv)^2 = A(hv - E_g), \hspace{3cm} (2)$$

where α denotes the absorption coefficient, A is a constant, h is the Planck constant, v is the frequency of the photon, and E_g is the optical bandgap. The intersection point between the extrapolation line and the x-axis represents the band gap of the Y_2O_3 film (a large optical band gap of 4.31 eV is observed in this case).

Figure 2 presents the XPS results of the fabricated Y_2O_3 film, with all binding energy values corrected to the main C 1s peak (284.8 eV). In Figure 2a, the XPS spectra for Y 3d reveal the two splitting orbitals, Y $3d_{5/2}$ and Y $3d_{3/2}$. The Y $3d_{5/2}$ and Y $3d_{3/2}$ peaks are located at 156.4 eV and 158.4 eV, respectively, confirming the successful formation of the Y_2O_3 film on the substrate. The XPS results of Y_2O_3 film for O 1s are shown in Figure 2b. The deconvoluted O 1s peaks appear at 529.0, 530.2, and 531.9 eV, corresponding to the oxygen lattice (O_L), oxygen vacancies (O_V), and hydroxyl group (-OH), respectively. The area ratio of the O_L peak was found to be 35.8%, while that of the O_V peak was 35.6%. These two components are almost equally proportioned in the O 1s spectra.
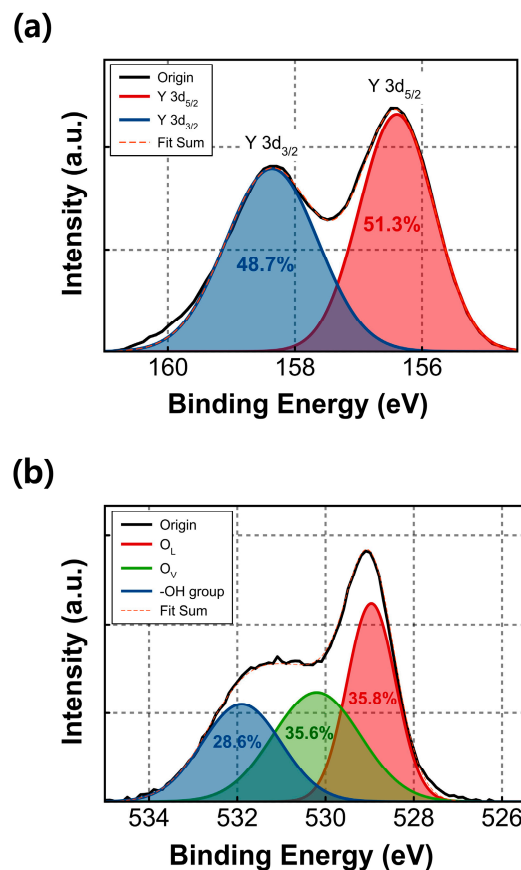

Figure 2. XPS spectra: (a) Y 3d and (b) O 1s of sol–gel-processed Y_2O_3 films.

Figure 3a presents a schematic image of the fabricated RRAM devices, the inset show the cross-sectional SEM image of Y_2O_3 films on ITO/glass substrates. Figure 3b displays representative I–V characteristics of the fabricated Y_2O_3 RRAM devices with different levels of compliance current. To observe the set/reset behavior, the voltage of the TE was swept from −15 V to 5 V, with the bottom electrode (BE) grounded. The read voltage was set at 0.1 V. The initially obtained resistance values were relatively high, indicating HRS. At a specific voltage known as the SET voltage, the current abruptly increased, resulting in low resistance values, referred to as the LRS. When a voltage was applied from positive to negative values, known as the RESET voltage, the LRS turned back into HRS. Importantly, all fabricated Y_2O_3-based RRAM devices demonstrated clear bipolar switching behavior

without requiring an unwanted forming process. This distinguishes them from O_V-rich metal oxide-based RRAMs or Ag/Cu electrode-based RRAMs, which often necessitate an additional forming process [21,22]. The Y_2O_3 films formed in this study exhibited some oxygen vacancy formation, and the use of Ag TE facilitated the easy formation of conductive filaments (CFs) without the need for a high voltage forming process. This mechanism is based on conductive bridge random-access memory, which operates through the reduction and oxidation of Ag. Comparisons were made between Y_2O_3 RRAM devices with Ag TE and those with Au TE. The RRAM with Au TE did not exhibit clear RRAM characteristics since Au cannot form conductive bridges similar to Ag due to its low reactivity [11]. In contrast, the diffusive nature of Ag allowed it to penetrate the switching layer easily, enabling the formation of CFs. Additionally, the Y_2O_3 switching layer contained abundant OV, which facilitated the formation of CFs without the need for applying a forming voltage. During the set process, a negative bias of −15 V was applied to the Ag TE, resulting in the HRS state. Upon applying a positive bias, Ag atoms lost electrons through an oxidation reaction and formed cations ($Ag \rightarrow Ag^+ + e^-$). These cations then migrated to the BE and received electrons through a reduction reaction ($Ag^+ + e^- \rightarrow Ag$), leading to the growth of reduced Ag atoms in the switching layer. Once a particular voltage was reached, the TE and the BE were connected by conductive bridges made of Ag, transitioning the device to LRS. An abrupt increase in current at the SET voltage corresponds to the set process. Conversely, when the voltage applied to the TE was swept toward −15 V, the current dropped suddenly at the RESET voltage. This is attributed to the oxidation reaction of the Ag atoms, facilitated by a thermal electrochemical process. The oxidized Ag cations then returned to the TE, causing the conductive bridges to dissolve, thereby disconnecting the TE and the BE and returning the device to its initial HRS state.
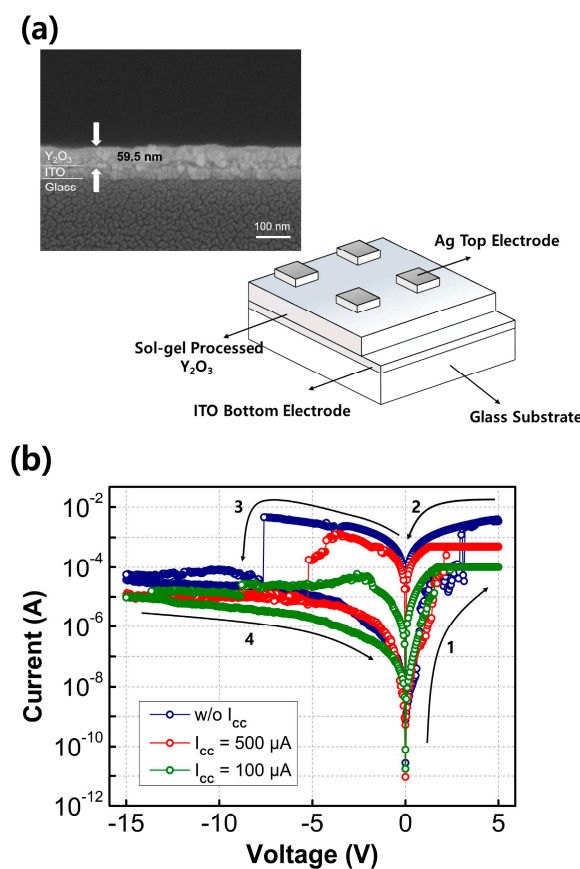

Figure 3. (a) Schematic of the device and the inset shows the cross-sectional SEM image of Y_2O_3 films on ITO/glass substrates and (b) representative IV curves of the fabricated Y_2O_3 RRAM, as a function of the set current compliance values.

Figure 4a illustrates the cumulative distribution function of the resistance states of the fabricated RRAM devices, programmed by setting different current compliance levels, with a read voltage of +0.1 V. As the current compliance values increased, the resulting resistance values gradually decreased, as shown in Figure CC. This led to the formation of intermediate resistance values within the LRS and HRS, rendering them suitable for MLC switching. The LRS values are influenced by factors such as the radius of the CFs or the concentration of filaments between the bottom and TEs [23,24]. When a low compliance current is applied to the device, the formation of CFs is suppressed, leading to narrower CFs and a slight increase in the resistance of the switching layer. Conversely, the HRS values did not exhibit significant changes, irrespective of the set current compliance value. The HRS values are known to be affected by the distance between the top of the broken CF and the TEs, known as the rupture region distance. The fact that the fabricated Y_2O_3 RRAM devices did not show significant HRS variation suggests that the rupture region distance between the top of the broken CF and the TEs was not affected by the set current compliance values.
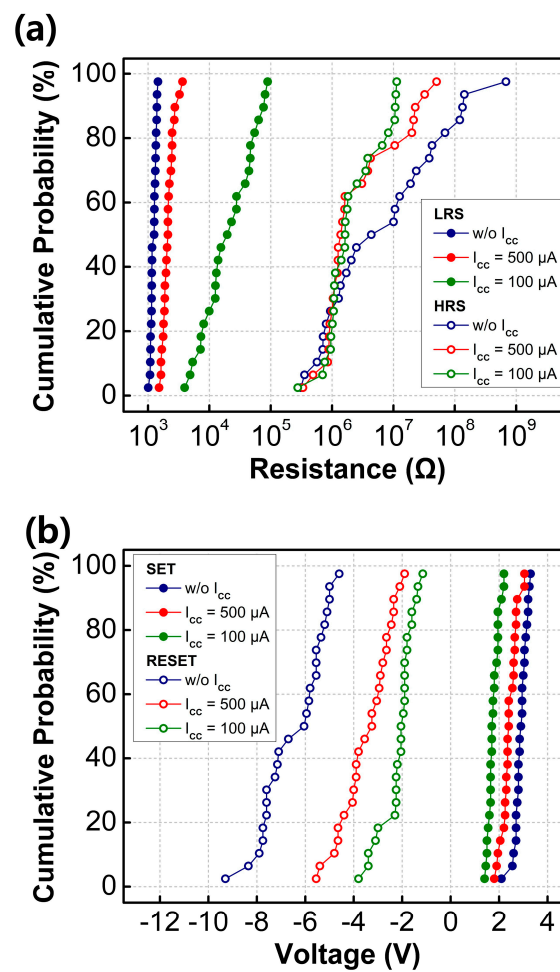
(a)

(b)

Figure 4. Cumulative distribution of resistance states (a) and SET and RESET values for sol–gel-processed Y_2O_3 RRAM devices.

As the set current compliance values increase, wider CFs are formed. Breaking thicker CFs, which result from the reduction process, requires larger RESET voltages. Consequently, as the set compliance current values increase, the RESET voltage also increases [25]. By controlling the current compliance values, the fabricated RRAM devices can operate as an MLC with a capacity of 2 bits in one cell through three LRSs and one common HRS.

To assess the reliability of the fabricated RRAM, endurance and retention tests were conducted under different compliance current conditions. The HRS and LRS values were extracted at a read voltage of +0.1 V. As shown in Figure 5a, the resistance states of the fabricated RRAM devices, both

with and without compliance current conditions, exhibited stable endurance properties for about 50 cycles. The largest on/off ratio was observed under compliance current-free conditions, with a value of around 10^3. Figure 5b displays the retention characteristics of the four resistance states. The three LRS and one HRS states exhibit excellent MLC behavior, maintaining their resistance values for up to 10^4 s without any significant degradation.
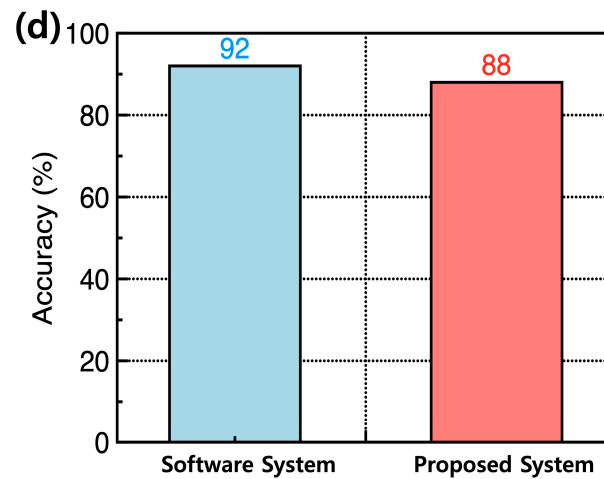
(a)

(b)

(c)
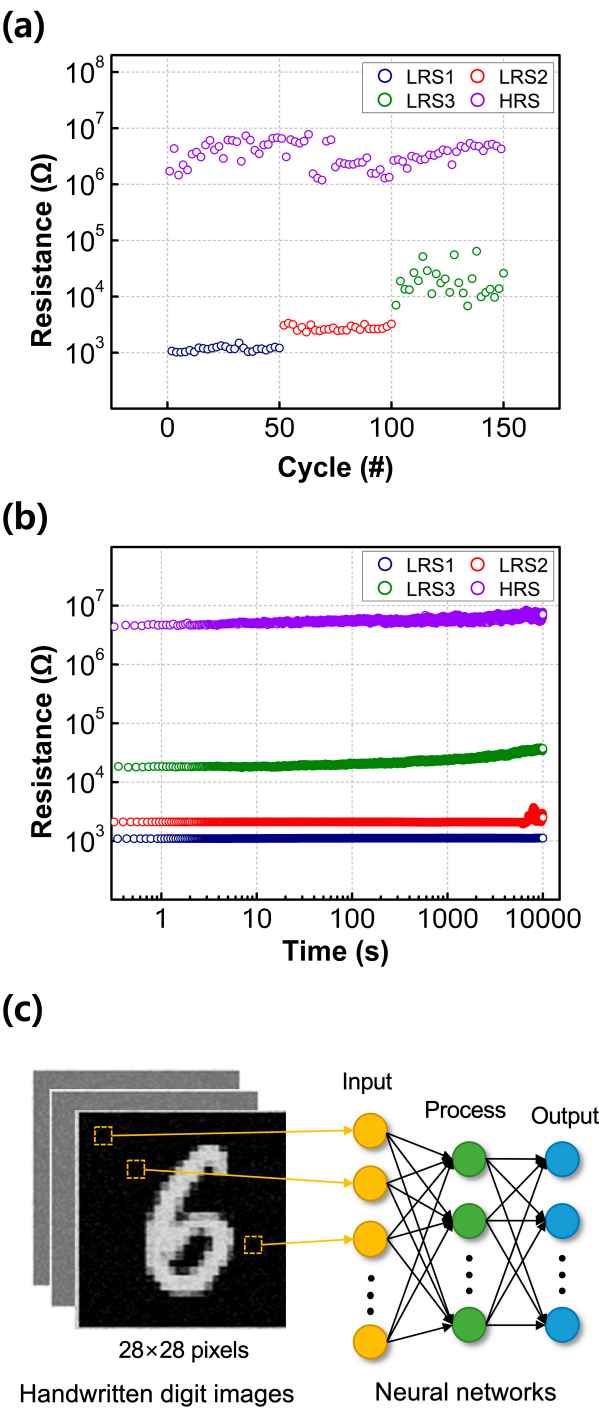
Figure 5. Non-volatile properties of sol–gel-process Y_2O_3 RRAM devices as a function of the set current compliance values: (a) endurance and (b) retention. (c) Constructed hardware neural network for classifying the hand written digit images provided by the Modified National Institute of Standards and Technology. The system is composed of three different neuron layers corresponding to the input (784 neurons), process (32 neurons), and output (10 neurons) signals. The neuron layers are interconnected through synaptic cells based on Y_2O_3 RRAM devices. (d) Recognition accuracy values for the ideal software system and the proposed hardware neural network. Each system was tested, after training for 60 epochs.

To assess the capability of the Y_2O_3 RRAM for neural networks, numerical simulations were conducted. Figure 5c illustrates the hardware systems, consisting of three distinct neuron layers, constructed to recognize handwritten digit images provided by the Modified National Institute of Standards and Technology. The system involved 784, 512, and 10 neurons for the input, processing, and output signals, respectively. The three layers of neurons were interconnected through artificial synapses. Each single synapse cell in the network comprised five different RRAM devices, and the non-volatile memory states of these devices were estimated based on the results shown in Figure 5c. During the training process, optimal distributions of synaptic weights were calculated through software simulation. These weights were then converted into feasible conductance values for the RRAM cell. Figure 5d displays the recognition accuracy of the constructed system after training for 60 epochs. The hardware neural networks based on the Y_2O_3 RRAM effectively classified the digit images with a high accuracy of approximately 88%, which is comparable to the ideal software-based recognition accuracy of about 92%. This demonstrates that the proposed Y_2O_3 RRAM can be utilized as a memory component to achieve practical neuromorphic systems.

4. Conclusions

Sol–gel-processed Y_2O_3 RRAM devices were successfully fabricated on ITO/glass substrates. These devices exhibit conventional bipolar RRAM characteristics, eliminating the need for a high voltage forming process. By increasing the set current compliance values, the resistance values obtained gradually decrease, allowing for the realization of intermediate resistance values within the LRS and HRS, rendering them suitable for MLC switching. The fabricated devices can effectively operate as an MLC with a capacity of 2 bits in one cell, utilizing three LRS and one common HRS. When applying a low compliance current to the device, the formation of CF is suppressed, leading to a narrower CF and a slight increase in the resistance of the switching layer. To evaluate the potential of the Y_2O_3 RRAM for neural networks, numerical simulations were conducted. The results demonstrate that hardware neural networks based on the Y_2O_3 RRAM effectively classify digit images with a high accuracy of about 88%. This indicates that the proposed Y_2O_3 RRAM can be utilized as a memory component to achieve practical neuromorphic systems.

References

1. Wang, Z.; Joshi, S.; Savel'ev, S.E.; Jiang, H.; Midya, R.; Lin, P.; Hu, M.; Ge, N.; Strachan, J.P.; Li, Z. Memristors with diffusive dynamics as synaptic emulators for neuromorphic computing. *Nat. Mater.* **2017**, 16, 101–108.
2. Yoon, J.H.; Wang, Z.; Kim, K.M.; Wu, H.; Ravichandran, V.; Xia, Q.; Hwang, C.S.; Yang, J.J. An artificial nociceptor based on a diffusive memristor. *Nat. Commun.* **2018**, 9, 417.
3. Jeong, D.S.; Hwang, C.S. Nonvolatile memory materials for neuromorphic intelligent machines. *Adv. Mater.* **2018**, 30, 1704729.
4. Bai, Y.; Wu, H.; Wu, R.; Zhang, Y.; Deng, N.; Yu, Z.; Qian, H. Study of Multi-level Characteristics for 3D Vertical Resistive Switching Memory. *Sci. Rep.* **2014**, 4, 5780.
5. Jang, J.; Subramanian, V. Effect of electrode material on resistive switching memory behavior of solution-processed resistive switches: Realization of robust multi-level cell. *Thin Solid Films* **2017**, 625, 87–92.
6. Smith, J.; Chung, S.; Jang, J.; Biaou, C.; Subramanian, V. Solution-processed complementary resistive switching arrays for associative memory. *IEEE Trans. Electron Devices* **2017**, 64, 4310–4316.
7. Lee, S.; Kim, T.; Jang, B.; Lee, W.Y.; Song, K.C.; Kim, H.S.; Do, G.Y.; Hwang, S.B.; Chung, S.; Jang, J. Impact of device area and film thickness on performance of sol-gel processed ZrO_2 RRAM. *IEEE Electron Device Lett.* **2018**, 39, 668–671.
8. Ha, S.; Lee, H.; Lee, W.Y.; Jang, B.; Kwon, H.J.; Kim, K.; Jang, J. Effect of annealing environment on the performance of sol-gel-processed ZrO_2 RRAM. *Electronics* **2019**, 8, 947.
9. Kim, K.; Hong, W.; Lee, C.; Lee, W.Y.; Kim, H.J.; Kwon, H.J.; Kang, H.; Jang, J. Sol-gel-processed amorphous-phase ZrO_2 Based resistive random-access memory. *Mater. Res. Express* **2021**, 8, 116301.
10. Ding, Z.; Feng, Y.; Huang, P.; Liu, L.; Kang, J. Low-power resistive switching characteristic in HfO_2/TiO_x bi-layer resistive random-access memory. *Nanoscale Res. Lett.* **2018**, 14, 157.
11. Kim, K.; Lee, C.; Lee, W.Y.; Kim, H.J.; Lee, S.H.; Bae, J.H.; Kang, I.M.; Jang, J. Enhanced switching ratio of sol–gel-processed Y_2O_3 RRAM device by suppressing oxygen-vacancy formation at high annealing temperature. *Semicond. Sci. Technol.* **2021**, 37, 015007.
12. Kim, D.W.; Kim, H.J.; Lee, W.Y.; Kim, K.; Lee, S.H.; Bae, J.H.; Kang, I.M.; Kim, K.; Jang, J. Enhanced switching reliability of sol–gel-processed Y_2O_3 RRAM devices based on Y_2O_3 surface roughness-induced local electric field. *Materials* **2022**, 15, 1943.
13. Kim, H.J.; Kim, D.W.; Lee, W.Y.; Kim, K.; Lee, S.H.; Bae, J.H.; Kang, I.M.; Kim, K.; Jang, J. Flexible sol-gel-processed Y_2O_3 RRAM devices obtained via UV/Ozone-assisted photochemical annealing process. *Materials* **2022**, 15, 1899.
14. Kim, H. I.; Lee, T.; Lee, W. Y.; Kim, K.; Bae, J. H.; Kang, I. M.; Lee, S. H.; Kim, K.; Jang, J. Improved Environment Stability of Y2O3 RRAM Devices with Au Passivated Ag Top Electrodes. *Materials* **2022**, 15 6859.
15. Kim, K.; Kim, H. I.; Lee, T.; Lee, W. Y.; Bae, J. H.; Kang, I. M.; Lee, S. H.; Jang, J. Thickness dependence of resistive switching characteristics of the sol–gel processed Y_2O_3 RRAM devices. *Semicond. Sci. Technol.* **2023**, 38, 045002.
16. Lee, C.; Lee, W.Y.; Kim, H.J.; Bae, J.H.; Kang, I.M.; Lim, D.; Kim, K.; Jang, J. Extremely bias stress stable enhancement mode sol–gel-processed SnO2 thin-film transistors with Y_2O_3 passivation layers. *Appl. Surf. Sci.* **2021**, 559, 149971.
17. Lee, Y.W.; Kim, D.W.; Kim, H.J.; Kim, K.; Lee, S.H.; Bae, J.H.; Kang, I.M.; Kim, K.; Jang, J. Environmentally and electrically stable sol–gel-deposited SnO_2 thin-film transistors with controlled passivation layer diffusion penetration depth that minimizes mobility degradation. *ACS Appl. Mater. Interfaces* **2022**, 14, 10558–10565.
18. Jang, J.; Kang, H.; Chakravarthula, H.C.N.; Subramanian, V. Fully inkjet-printed transparent oxide thin film transistors using a fugitive wettability switch. *Adv. Electron. Mater.* **2015**, 1, 1500086.

19. Scheideler, W.J.; Jang, J.; Karim, M.A.U.; Kitsomboonloha, R.; Zeumault, Z.; Subramanian, V. Gravure-Printed Sol-Gels on Flexible Glass: A Scalable Route to Additively Patterned Transparent Conductors. *ACS Appl. Mater. Interfaces* **2015**, 7, 12679–12687.

20. Lim, D. G.; Kwak, D. J.; Yi, J. Improved interface properties of yttrium oxide buffer layer on silicon substrate for ferroelectric random access memory applications. *Thin Solid Films* **2017**, 422, 150–154.

21. Yang, B.; Xu, N.; Li, C.; Huang, C.; Ma, D.; Liu, J.; Arumi, D.; Fang, L. A forming-free ReRAM cell with low operating voltage. *IEICE Electron. Express* **2020**, 17, 20200343.

22. Abbas, Y.; Ambade, R.B.; Ambade, S.B.; Han, T.H.; Choi, C. Tailored nanoplateau and nanochannel structures using solution-processed rutile TiO_2 thin films for complementary and bipolar switching characteristics. *Nanoscale* **2019**, 11, 13815.

23. Prakash, A.; Deleruyelle, D.; Song, J.; Bocquet, M.; Hwang, H. *App. Phys. Lett.* **2015** 106, 233104.

24. Sedghi, N.; Li, H.; Brunell, I. F.; Dawson, K.; Potter, R. J.; Guo, Y.; Gibbon, J. T.; Dhanak, V. R.; Zhang, W. D.; Zhang, J. F.; Robertson, J.; Hall, S.; Chalker, P. R.; The role of nitrogen doping in ALD Ta_2O_5 and its influence on multilevel cell switching in RRAM. *App. Phys. Lett.* **2017,** 110, 102902.

25. Kim, D.; Shin, J.; Kim, S. Resistive Switching Characteristics of ZnO-Based RRAM on Silicon Substrate. *Metals* **2021**, 11, 1572.